Impacts of Biofuel Blending on MCCI Ignition Delay with Review of Methods for Defining Cycle-by-Cycle Ignition Points from Noisy Cylinder Pressure Data

Preprint

Jonathan Martin, Jonathan Burton, Jon Luecke, and Robert L. McCormick

National Renewable Energy Laboratory

Presented at the SAE WCX World Congress Experience Digital Summit
April 13–15, 2021

NREL is a national laboratory of the U.S. Department of Energy
Office of Energy Efficiency & Renewable Energy
Operated by the Alliance for Sustainable Energy, LLC

This report is available at no cost from the National Renewable Energy Laboratory (NREL) at www.nrel.gov/publications.

Contract No. DE-AC36-08GO28308

Conference Paper
NREL/CP-5400-78762
April 2021

Impacts of Biofuel Blending on MCCI Ignition Delay with Review of Methods for Defining Cycle-by-Cycle Ignition Points from Noisy Cylinder Pressure Data

Preprint

Jonathan Martin, Jonathan Burton, Jon Luecke, and Robert L. McCormick

National Renewable Energy Laboratory

Suggested Citation
Martin, Jonathan, Jonathan Burton, Jon Luecke, and Robert L. McCormick. 2021. *Impacts of Biofuel Blending on MCCI Ignition Delay with Review of Methods for Defining Cycle-by-Cycle Ignition Points from Noisy Cylinder Pressure Data: Preprint*. Golden, CO: National Renewable Energy Laboratory. NREL/CP-5400-78762.
https://www.nrel.gov/docs/fy21osti/78762.pdf.

Conference Paper
NREL/CP-5400-78762
April 2021

National Renewable Energy Laboratory
15013 Denver West Parkway
Golden, CO 80401
303-275-3000 • www.nrel.gov

Impacts of Biofuel Blending on MCCI Ignition Delay with Review of Methods for Defining Cycle-by-Cycle Ignition Points from Noisy Cylinder Pressure Data

Jonathan Martin, Jonathan Burton, Jon Luecke, and Robert L. McCormick

Abstract

Conventional diesel combustion, also known as Mixing-Controlled Compression Ignition (MCCI), is expected to be the primary power source for medium- and heavy-duty vehicles for decades to come. Displacing petroleum-based ultra-low-sulfur diesel (ULSD) as much as possible with low-net-carbon biofuels will become necessary to help mitigate effects on climate change. Neat biofuels may have difficulty meeting current diesel fuel standards but blends of 30% biofuel in ULSD show potential as 'drop-in' fuels. These blends must not make significant changes to the combustion phasing of the MCCI process if they are to be used interchangeably with neat ULSD. An important aspect of MCCI phasing is the ignition delay (ID), i.e. the time between the start of fuel injection and the initial premixed autoignition that initiates the MCCI process. Bench experiments can evaluate the expected ignition delay of a fuel via cetane number (CN) or alternative methods such as the indicated cetane number (ICN); however, neither CN nor ICN correlate perfectly with the ignition delay measured in actual engine experiments. Furthermore, there is no standardized methodology on how to quantify MCCI ignition delay from engine cylinder pressure measurements, creating difficulties in cross-study comparison. In this study, several engine ignition delay calculation methods are evaluated for robustness in deriving ignition delay on both a cycle-averaged and cycle-to-cycle basis. Eight biofuel blends with varying ICN, oxygen concentration and other fuel properties were used to study the different methods. This yields a thorough analysis of how certain biofuel blends affect ignition delay and the entire MCCI process, as well as a thorough evaluation of the differences between the ID calculation methods. Many of these methods are equally valid, but the choice of method has a significant impact on the resulting ID, which must be carefully considered when evaluating results across multiple studies.

Introduction

The primary driver of climate change is the emission of carbon dioxide (CO_2) from combustion-based energy sources [1]. Although there has been much progress in recent decades shifting to non-combustion energy sources, combustion of fossil fuels still accounts for 85% of global energy consumption [2]. The US Energy Information Administration (EIA) projects that combustion of liquid fuels will still account for 30% of world energy consumption in 2040, barely reduced from 33% in 2012 [3]. It is therefore imperative to find biomass-based substitutes for petroleum-derived fuels that can be mixed in with the current fuel supply without significant adverse effects on performance. These biofuels can have low net CO_2 emissions and their carbon mitigation potential (with some pathways even showing the promise of *negative* net carbon) makes them an essential tool in combating climate change [4]. Biofuels could also benefit US energy security by making fuel prices less vulnerable to crude oil supply shocks [5].

The light-duty vehicle market is shifting to hybridization and full electrification to reduce net CO_2 emissions [6]. Electrification of commercial medium-to-heavy-duty vehicles is more difficult given their typical operating drive cycles and distances, high power demands, duty cycles, and recharge speed demands [7]. The dominant energy source for these vehicles is petroleum-derived diesel fuel used in compression-ignition (CI) engines or "diesel" engine [8]. Although there are many advanced combustion modes for CI engines currently being developed [9,10,11], commercial CI engines currently use the conventional combustion mode of Mixing-Controlled Compression Ignition (MCCI), which while very efficient, inherently produces high engine-out emissions of nitric oxides (NO_X) and soot [12]. Some biofuels have shown potential to reduce these emissions among their other benefits [13]. Exhaust aftertreatment catalyst systems are currently used in vehicle exhaust systems to prevent these emissions from escaping into the atmosphere, however these systems have functionality limitations and add significant cost to the vehicle [14].

The cetane number (CN) is a critical property for an MCCI fuel that is defined by how quickly the fuel will ignite when injected into a pressurized CI engine chamber [15]. CN is inversely proportional to the time gap between the start of injection (SOI) and ignition, known as ignition delay (ID) [16,17]. A sufficiently short ID (and hence sufficiently high CN) is required to ensure that excess fuel vapor does not accumulate before ignition, resulting in rapid burning and engine knock [15]. The use of a neat biofuel may cause significant changes in CN/ID [18], which would require changes in engine calibration for engine to operate properly. However, a mid-level blend of biofuel and ULSD may not cause such problems and has the potential to serve as a "drop-in" substitute for neat diesel [19]. If a biofuel can increase CN (and reduce ID) in a blend with ULSD, it could eliminate the need for costly synthetic cetane improvers such as 2-ethyl hexyl nitrate (2-EHN), which has long been added to diesel fuel [20].

The correlation between fuel CN and engine ID can be poor, especially with oxygenated biofuels [21,22]. Official CN values are measured in a specially-designed fuel rating engine [23] with a more tightly controlled environment, lower bulk cylinder charge temperatures and pressures, and much lower injection pressure (~100 bar) than applied in modern on-road CI engines in typical operating conditions. This mismatch also applies to the alternative methods of *indicated* cetane number (ICN) and *derived* cetane number (DCN), and the discrepancy between these three values (CN, ICN, and DCN) can become very large with biofuels [24]. While there are standardized procedures for measuring CN, ICN, and DCN, there is no such standard for measuring ID in a modern on-road engine or equivalent test engines. Methods vary widely between research groups making it difficult to perform meta-analysis of results across different studies. It is also common practice for ID to be calculated from measurements that are averaged over many engine cycles, but this eliminates information on the magnitude of the variability for ID from cycle to cycle.

The goals of this paper are to (1) analyze and compare different engine ignition delay measurement methods proposed across literature, (2) select the method most suitable for studying how ignition delay changes in terms of both average and cycle-to-cycle variance, and (3) apply this method to determine the effects on biofuel blends for both the average and the cycle-to-cycle ID. This will investigate the plausibility of various biofuel blends to be used as drop-in diesel substitutes and attempt to foresee challenges in the adoption of these fuels due to changes in ignition behavior not apparent from standard CN measurements. The biofuel blendstocks used in this study were screened for suitable properties by Fioroni et al. [19], including

combustion properties of the pure compounds, such as lower heating value (LHV) and CN, as well as engine compatibility properties of blends with diesel, such as lubricity and conductivity. This study, along with a simultaneous companion study focusing on NO_X and soot emissions [13], aims to verify performance of some of the blends that passed the screening process in a commercial engine.

Methods

Fuel/Engine Selection

The fuels used in this study, identified in Table 1, were blended at 30% volume concentration with 70% EPA certification ultra-low-sulfur diesel (ULSD). Although many more blendstocks than the eight tested here passed the first two tiers of screening, these eight were selected to represent a wide variety of chemical functional groups while staying within budget and time limitations. The selected biofuels include a novel hydrocarbon biofuel derived from waste biomass via hydrothermal liquefaction (HTL) from Pacific Northwest National Laboratories (PNNL), a fuel whose production is detailed by Zacher et al. [25,26] and whose properties are detailed in the companion study by Burton et al. [13]. All fuels are expected to be readily compatible with commercial CI engines at this 30% blend level, with the possible exception of the polyoxymethylene ether (POME) mixture blend [27].

Table 1.Fuel blend indicated cetane number (ICN) per ASTM D8183. All blends are 30% bioblendstock, 70% certification ULSD. Properties of 100% ULSD are given in first data row. *Starred fuels are pure chemical compounds; the rest are complex mixtures detailed further in [13].

Blendstock		Blend of 30% vol. blendstock, 70% vol. ULSD			
Name	Group	Blend Short ID	ICN Trial 1	ICN Trial 2	ICN Average
Certification ULSD	Hydro-carbons	Cert	40.2	40.7	40.45
Renewable Diesel		RD30	50.9	51.0	50.95
Waste HTL (PNNL)		PN30	47.0	47.4	47.20
Soy Biodiesel	Esters	BD30	43.6	43.7	43.65
*Methyl Decanoate		MD30	45.1	45.0	45.05
*Hexyl Hexanoate		HH30	41.6	41.5	41.55
*1-Decanol	Alcohol	DL30	44.0	44.2	44.10
*Isoamyl Ether	Ethers	IE30	46.3	46.3	46.30
Polyoxymethylene Ether (POME) Mix		OM30	46.7	46.6	46.65

Indicated cetane numbers (ICN) shown in Table 1 for each blendstock were measured in duplicates using ASTM D8183 methodology with a Bosch CRI3-18 injector. For this method an Advanced Fuel Ignition Delay Analyzer (AFIDA) constant-volume combustion chamber relates measured ID time to ICN, calibrated with primary reference fuel (PRF) volumetric blends of n-hexadecane and 1-methylnaphthalene (which define cetane number) over the range of 35-85. Repeatability and reproducibility for samples with ICN 45 are reported to be 0.8 and 1.7, respectively [28].

Table 2.Test engine specifications.

Displacement single cylinder	831 cc	Base engine model	Ford Powerstroke® 6.7L Scorpion (MY2017)
Stroke	108 mm	Coolant inlet temp	90° C
Bore	99 mm	Oil temperature	90° C
Conrod length	177 mm	Fuel injector model	Bosch CRI3-20 (piezo)
Comp. ratio	16.2:1	Injection orifice size	0.138mm
No. of valves	4	Injector umbrella angle	150°
EVC	-329°	Injector # of holes	8
IVC	-133°	Cyl. pres. transducer	Kistler 6058A
EVO	114°	Charge amplifier	Kistler 5010
IVO	339°	Crank angle encoder	BEI 3600 count (0.1° res)

The engine used for this study, detailed in Table 2, is a custom-built single-cylinder CI engine modeled after the Ford Powerstroke® 6.7L Scorpion engine, with an OEM piston, crank, fuel rail, injector, and valve timing and an OEM-designed cylinder head with modifications for single-cylinder operation. The piezoelectric fuel injector is from the same model series (CRI3) used in the AFIDA and is thus expected to produce similar ignition delay behavior, but it should be noted that even injectors of identical model can produce different ignition delays due to factors such as aging, manufacturing tolerances, and the different temperatures/pressures found in the AFIDA and the engine.

Further differences can be caused by the injection pressures and durations used at the engine operating conditions, which differed from the constant conditions of 1000 bar and 1.5 ms used in ICN tests. Three speed/load conditions were selected to cover a wide range of the engine's typical operating envelope, with each condition given a letter/number nickname representing speed/load. "A20" represents a near-idle condition, while "D40" represents a cruise condition, and "G60" represents moderate acceleration. The setpoints of actively controlled parameters at these conditions are given below in Table 3. Two parameters were varied in a five-point sweep to test sensitivity: the level of exhaust gas recirculation (EGR) and the SOI timing of the main injection. The "base" value of these two parameters (used while the other parameter is swept) is given in parentheses in Table 3.

Table 3. Engine test conditions. *Total EGR and main injection SOI were varied over a sweep, the range of the sweep is given with the base value in parentheses. **Main injection duration was varied to maintain constant load.

Condition nickname	"A20"	"D40"	"G60"
Engine speed, RPM	600	1300	2075
Engine load, bar gIMEP	3.3	6.45	9.8
Intake air pressure, bar abs	1.05	1.23	1.80
Intake air temperature, °C	50	53	73
Exhaust backpressure, bar abs	1.2	1.5	2.5
*Total EGR, % (base)	25 to 37 (25)	11 to 31 (31)	18 to 26 (26)
Fuel rail pressure, bar	350	1400	1600
Pilot injection #2 SOI, °aTDC	-19.8	N/A	N/A
Pilot injection #2 duration, ms	0.230	N/A	N/A
Pilot injection #2 mass, mg	~0.5	N/A	N/A
Pilot injection #1 SOI, °aTDC	-10.7	-13.2	-21.0
Pilot injection #1 duration, ms	0.450	0.227	0.198
Pilot injection #1 mass, mg	~4.0	~2.4	~1.6
*Main injection SOI, °aTDC	-1.4 to 10.6 (-1.4)	-2.5 to 5.5 (1.5)	-8.2 to -0.2 (-0.2)
**Main injection duration, ms	~0.78	~0.53	~0.64
Main injection mass, mg	~13.4	~24.7	~37.5

Cylinder Pressure Measurement

The in-cylinder pressure transducer was installed in a port in the cylinder head that runs parallel with the fire deck. The center line of the port is 6.5mm above the fire deck. The port enters the combustion chamber through a 3 mm hole that is 90° to the transducer and is 37 mm from the center line of the cylinder/injector. The pressure transducer, given in Table 2, is a piezo-electric type and uses a charge amplifier to convert the charge into a voltage signal. The signal is measured and recorded by a DRIVVEN DAQ/ECU-emulating cart. This signal, along with multiple other critical signals required for combustion analysis, were recorded at a rate of 3600 points per revolution of the engine, a resolution of 0.1° crank angle (CA).

There are many potential signal noise sources for the high-speed in-cylinder pressure data. This noise must be filtered out to enable effective and robust cylinder pressure analysis. The noise filtering method selected for this study is the cubic smoothing spline, using the "SMOOTH" routine originally developed by de Boor [29]. This method converts the discrete signal sampled at 0.1° CA into a

continuous function. Smoothing parameter S is adjusted to achieve the desired smoothing, ranging from a pure point-to-point spline interpolant with no smoothing at S=0 and a pure linear fit at S=1. This parameter is named p by de Boor but changed to S in Figure 1 so that p can represent pressure. A raw pressure signal from condition D40 is shown smoothed with 3 different values of S. Also shown is error E between the raw and smoothed signals, the measured injector current signal, and a modeled fuel flow rate (generated from OEM injector flow data).

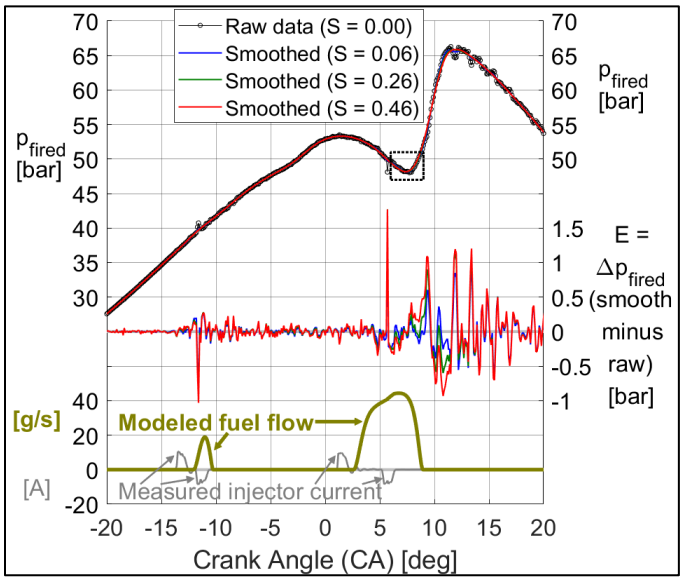

Figure 1. Cylinder pressure smoothing for the D40 condition.

It is difficult to see the differences between the three values of S in Figure 1. Figure 2 zooms in on the most pertinent section of the pressure trace for this study, the location of ignition for the main fuel injection event around 6-9° CA. At ignition, the pressure trace deflects upward, and the value of S must not "round off" this deflection while still eliminating noise. The value of 0.46 is too great, clearly deflecting from the original data after ignition, but not 0.26 and 0.06. In the next section, derivatives of this signal are used to evaluate ignition, showing that S = 0.06 is too small. This "happy medium" value of 0.26 will be used for further analysis.

A quantitative method was developed to optimize S for each of the 3 engine speed/load conditions. The total absolute error $\Sigma|E|$ was calculated along with its derivative with respect to S while sweeping from S = 0 to S = 1 in increments of 0.01. The minima of this function were used to select S; see Figure 3. From anecdotal observations these values provided good balance between noise elimination and minimal signal distortion. A higher S is needed for higher speed/load conditions where more noise is present.

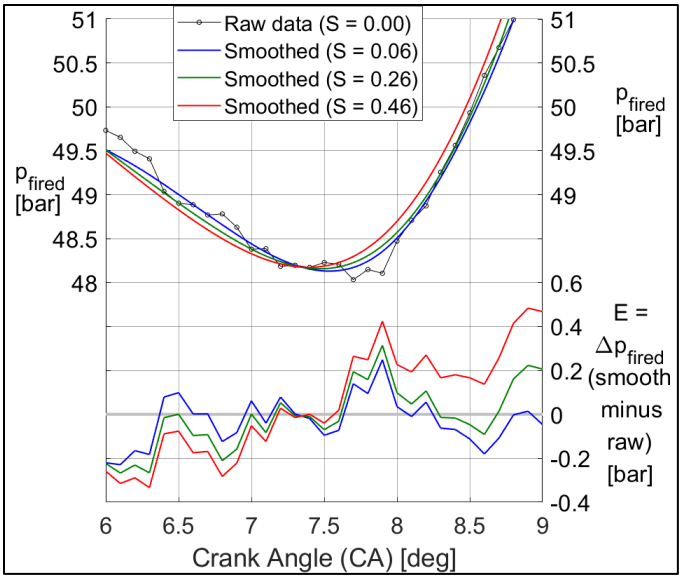

Figure 2. Cylinder pressure smoothing in the D40 condition, zoomed in on the point for ignition of the main fuel injection event. S = 0.46 causes too much deflection which would result in erroneous calculations of ID.

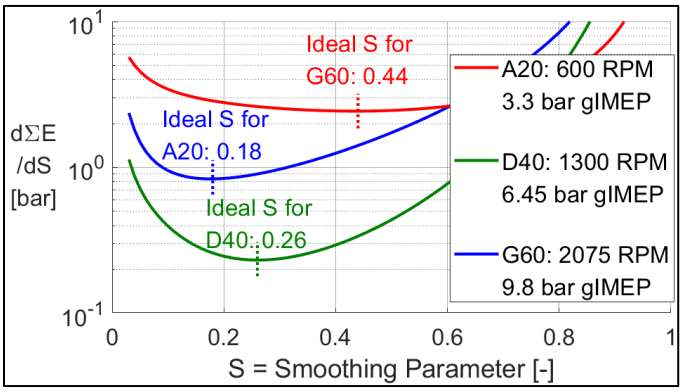

Figure 3. Minimizing the error for selecting smoothing parameter S.

Cylinder Pressure Calculus for HRR and Derivatives

Smoothed cylinder pressure p is used to calculate *apparent* heat release rate (AHRR) using instantaneous cylinder volume V as a function of crank angle θ, with a constant ratio of specific heats γ = 1.34 [30]:

$$\text{AHRR} = \frac{dQ}{d\theta} = \frac{\gamma}{\gamma-1} p \frac{dV}{d\theta} + \frac{1}{\gamma-1} V \frac{dp}{d\theta} \quad (1)$$

As Figure 4 shows, it is important that smoothing is applied not just initially to the raw cylinder pressure but also re-applied after every derivative. Fluctuations are amplified with each successive derivative, and these fluctuations are minimized when re-applying the smoothing after each derivative, creating a usable signal. The 5-point stencil was used for all derivatives in this study [31]:

$$f'(x) \approx \frac{-f(x+2h)+8f(x+h)-8f(x-h)+f(x-2h)}{12h} \quad (2)$$

In Equation (2), h is the step size of the function. For smoothed cylinder pressure and all its derivatives, h = 0.01° CA, and the smoothed cylinder pressure thus has 10x the resolution of the original pressure signal, sampled at intervals of 0.1° CA. This reduces discretization of the calculated ID vs. the coarse 0.1° sampling interval.

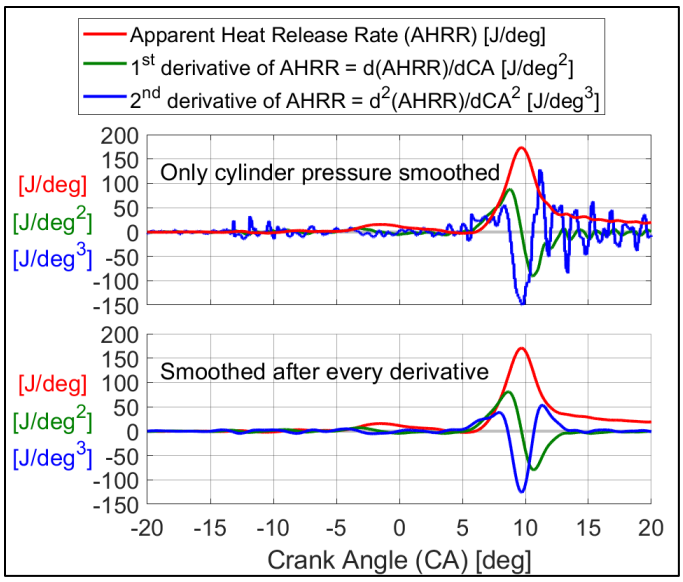

Figure 4. Comparing AHRR and its derivatives when smoothing is only applied to the raw cylinder pressure (top) and when smoothing is also re-applied after each derivative is taken (bottom). Pressure data from the D40 operating condition shown.

Details of AHHR caused by fuel injection and two-stage ignition, possible low temperature heat release (LTHR) and high temperature heat release (HTHR), are shown in Figure 5. There is a pilot injection for this condition but details of that are not shown on this plot, though the end of the AHHR curve is visible from 0° to 2° CA. When $S = 0.06$ the evaporation cooling effect from the main fuel injection can be seen as the AHRR drops at 3° CA and then a hypothesized LTHR can be seen as the curve flattens around 4° CA, whereas these details are filtered out for the $S = 0.26$ and $S = 0.46$ cases. LTHR is not very relevant to MCCI operation where the HTHR dominates combustion. However, it is relevant that smoothing shifts the apparent start point of HTHR slightly backward. An ideal ID-finding method would find an ignition point near the apparent HTHR start at ~6° CA.

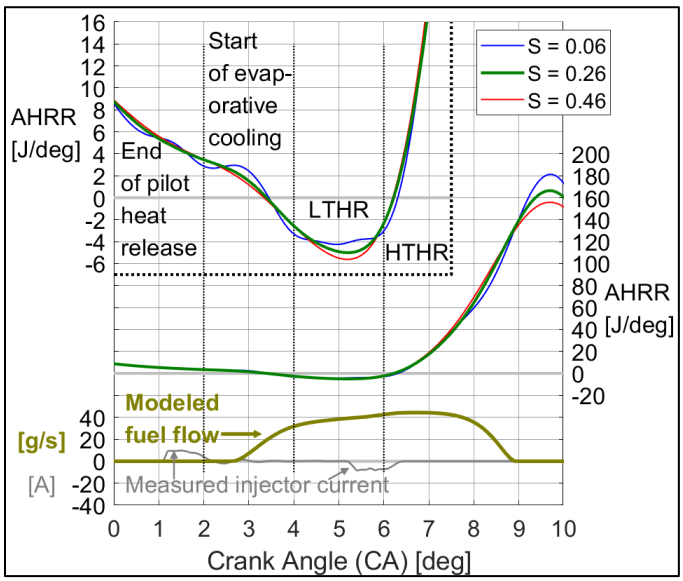

Figure 5. D40 AHRR with various values of smoothing parameter S, zoomed in to show detail of main injection ignition.

Review of Methods for Defining Start of Injection and Point of Ignition

Calculating ignition delay requires quantifying two points: the start of injection and the location of ignition. The start of injection was defined as the time when fuel first begins exiting the nozzle orifice. For this experimental setup the start of injection was defined as 0.12 ms after the measured injector current crossed the threshold of 1 A. This value of 0.12 ms was derived from pressure traces from the AFIDA, which show onset of pressure fluctuations at 0.12 ms after the 1 A current threshold [32], and confirmed by in-cylinder pressure measurements. The AFIDA uses a similar Bosch CRI3-series piezoelectric injector as used in the experimental engine. Various methods were researched from literature to define the location of ignition. Four methods were chosen for comparison from well-established engine research groups and a fifth method was created to emulate the ICN testing process. All five methods are applied to the same engine cycle from the D40 operating condition used in Figure 5.

Method A ("Positive AHRR" Method)

An AHRR method used by Mueller [33] is referred to herein as Method A. This method defines the point where AHRR first becomes positive as the point of ignition, as shown in Figure 6. This can be done using either the AHRR or a corrected HRR in which the AHRR of a motoring test at the same conditions is calculated to correct for heat transfer loss to the cylinder walls, engine head and piston. Heat of vaporization (HOV) of the liquid fuel as it evaporates causes the HRR to dip below zero. As fuel ignition occurs the HRR increases above zero which is the key threshold for this method. As a result, this method can be susceptible to shifts in the calculated start of ignition location based on the HOV of the fuel. Residual heat from combustion of the pilot injection can also bias the point of ignition. This is not meant as a criticism of the method, since it will be seen that all the following methods have their own unique drawbacks, and there is no perfect method given the imperfect nature of HRR calculation.

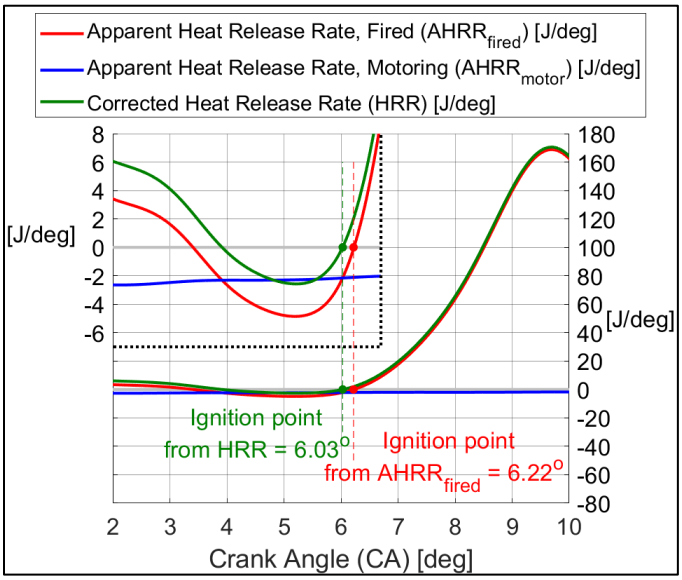

Figure 6. Method A of determining ignition point from AHRR.

Method B ("Tangent Line" Method)

Rothamer et al. [16] also compared five common ID calculation methods and selected the method presented below as producing the results most similar to all other methods. This method produced ignition delays in the middle of the range of the five methods studied

and was chosen to match typical ignition delay data available in literature. The first step of this method is to find the *motor-corrected* cylinder pressure p_{cor}, which is defined as the fired pressure trace p_{fired} minus a cycle-averaged motoring pressure trace p_{motor}. The peak of the 1st derivative for p_{cor} is then found, as shown in Figure 7. A line tangent to p_{cor} at this peak of the 1st derivative, which is point of maximum slope for p_{cor}, is then extrapolated downward. The intersection of this tangent line with zero is defined as the point of ignition.

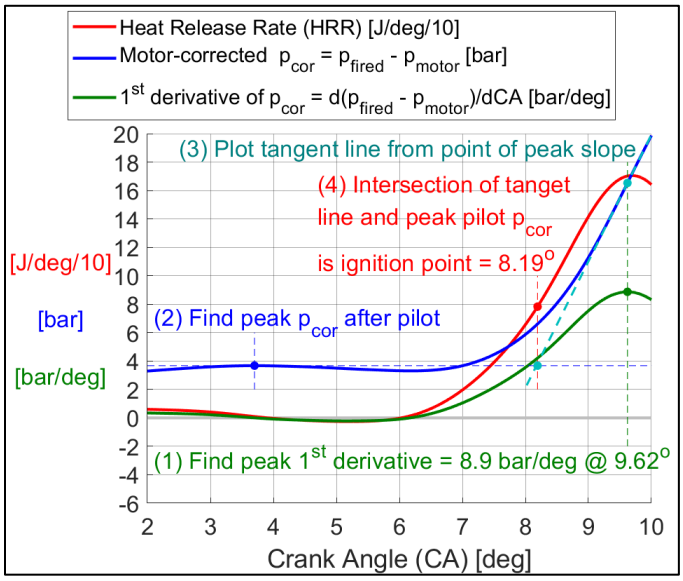

Figure 7. Method B of determining ignition point from 1st derivative of cylinder pressure.

For the current study, which features realistic multi-injection test conditions, the original method must be modified since zero is meant to be baseline pressure at SOI. Thus, a step must be added to find the peak p_{cor} produced by the pilot and use this as the baseline instead. The original method has the advantage of not being influenced by HOV, but in this modified method the HRR dip caused by evaporative loss after a pilot injection will influence the location of the initial peak in p_{cor}. This modified method will be referred to herein as Method B.

Method B places ignition later than Method A, after HTHR has begun, which is common throughout the literature as shown by the other methods reviewed by Rothamer et al. [16]. However, since MCCI does not feature a single discrete ignition event, rather stochastic autoignition throughout complex, chaotically mixed fuel/air spray plumes (typically from several individual fuel jets) and multiple ignition events, the ignition delay need not be defined at the very start of HTHR. The current study at hand focuses on the *difference* in ignition delay between fuels, so it is more important that the method produce ignition points that are *consistent* in their location relative to the larger MCCI process, regardless of fuel or test condition.

Method C ("2nd Derivative Peak" Method)

A method developed by Assanis et al. [17] simply uses the peak in the 2nd derivative of cylinder pressure as the point of ignition, which will be referred to herein as Method C. There is very little difference between the corrected and uncorrected 2nd derivative, and in the example shown in Figure 8, there was no change in the point of ignition when corrected or uncorrected pressure was used, at least at this level of precision (0.01° CA). This method is still not free of influence from the fuel HOV, since the sudden loss of fuel flow at the end of injection will cause a sudden end to evaporative loss and accelerate the pressure rise, pushing the 2nd derivative upward. Looking back at modeled fuel flow in Figure 5, it appears that this happens almost simultaneously with the 2nd derivative peak in the same cycle shown in Figure 8. However, HOV should still exert less influence over the 2nd derivative than the 1st derivative used by Methods A and B. (Method A uses HRR, which is calculated from the 1st derivative of cylinder pressure).

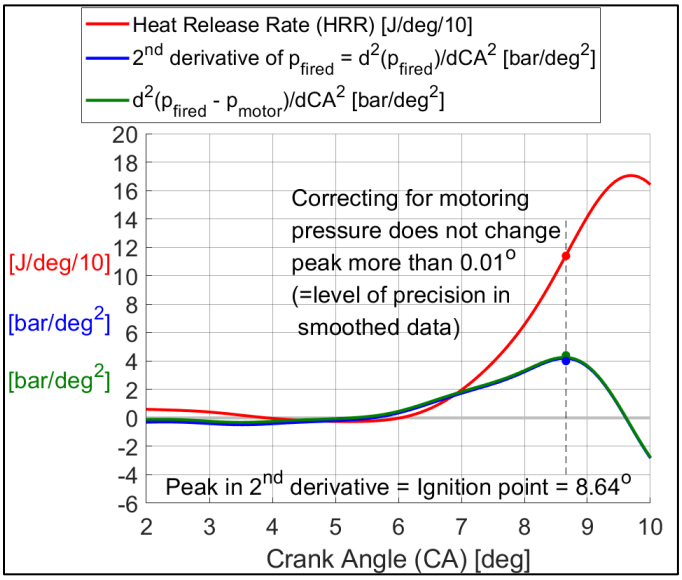

Figure 8. Method C of determining ignition point from 2nd derivative of cylinder pressure.

Method D ("HRR Curvature" Method)

As part of a larger effort to produce a comprehensive heat release analysis software, Ortiz-Soto et al. developed a method to quantify ignition points in advanced HCCI and SACI engines [34], where ID is much more ambiguous and variable than in MCCI. Although not designed specifically for MCCI, this method could have the advantage of being a "universal" ignition point method that can be applied to all CI modes and advanced multi-mode strategies. This method, referred to herein as Method D, requires computing the 1st and 2nd derivatives of HRR, which effectively uses the 3rd derivative of cylinder pressure. Computing this high order derivative and maintaining a meaningful signal requires careful treatment of the raw data and numerical differentiation methods, as illustrated previously in Figure 4. This enables calculation of the curvature k of the normalized HRR_{nor} via the following equation [35]:

$$k = \frac{\frac{d^2(\mathrm{HRR_{nor}})}{d\theta^2}}{\left(1+\frac{d(\mathrm{HRR_{nor}})^2}{d\theta}\right)^{\frac{3}{2}}} \quad (4)$$

It is important to note that curvature will change (not just in scale, but in the shape of the profile) depending on the units used for each axis. For Method D, the x-axis is left in units of degrees CA, while the y-axis (HRR_{nor}) is normalized to units of inverse rotations:

$$\mathrm{HRR_{nor}}[rot^{-1}] = \frac{\mathrm{HRR[J/deg]}*360[\mathrm{deg/rot}]}{\int_{SOI}^{100^\circ} \mathrm{HRR[J/deg]}d\theta[\mathrm{deg}]} \quad (5)$$

The ignition point is then defined as the average of the peak in the second derivative of HRR_{nor} and the peak of its curvature, putting the ignition point very close to the start of HTHR, as seen in Figure 9.

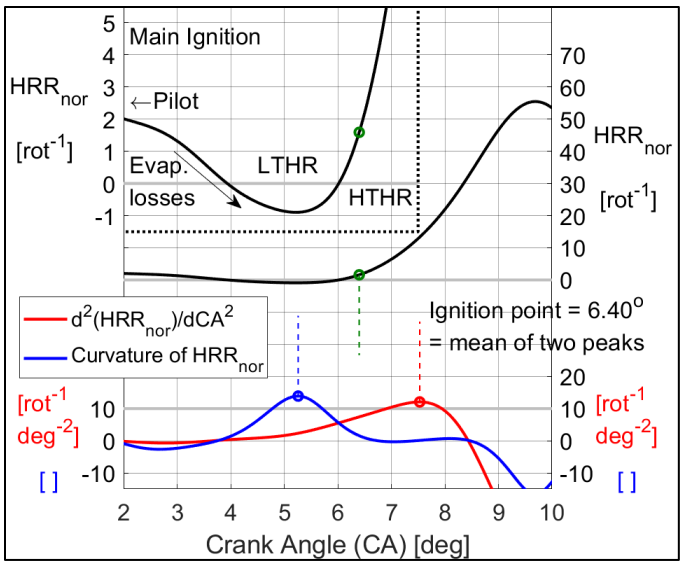

Figure 9. Method D of determining ignition point from normalized HRR (Equation 5), using its 2nd derivative and curvature (Equation 4).

One advantage of Method D is that this same process can identify other key points in the MCCI process, including the *end* of premixed autoignition, and thus measure changes in the *duration* of the premixed ignition phase. Figure 10 zooms in on the pilot ignition showing negative temperature coefficient (NTC) behavior between LTHR and HTHR, and the start of both LTHR and HTHR are identified.

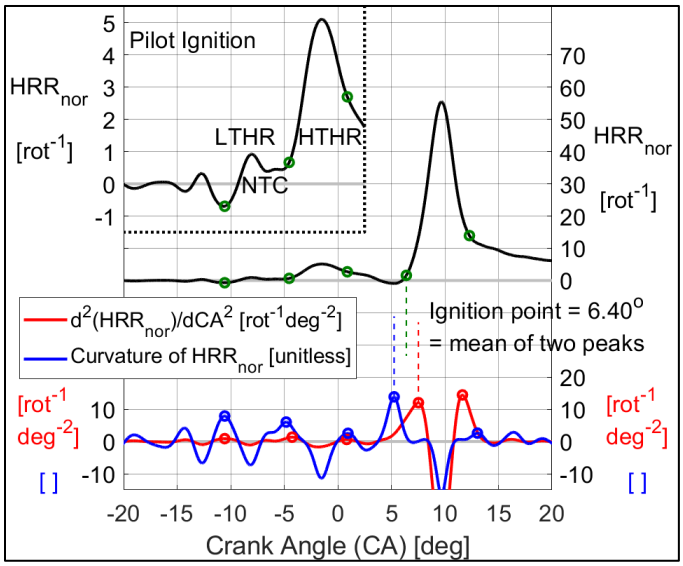

Figure 10. Method D identifies both start and end of premixed phases.

Method E ("ICN-Imitating" Method)

To correlate ID with CN, it is prudent to have an ignition point method that matches the CN method as much as possible. The AFIDA ICN used here is measured with a similar injector as the engine, but in a constant-volume chamber, defining ignition from pressure alone. Per ASTM D8183 [28], ICN is the average of two points: ID_0, the point where the fired pressure crosses the initial baseline pressure, and ID_{150}, the point where the fired pressure reaches 150 kPa above the baseline pressure. The pressure from constant-volume ICN testing is analogous to the mass fraction burned (MFB) of an engine: the integral of HRR, normalized by total integrated heat released over the cycle. The start and end of the MFB integration were set at SOI (before evaporative loss) and 100° CA (latest observed combustion):

$$\mathrm{MFB}(\theta) = \frac{\int_{SOI}^{\theta} HRR\, d\theta}{\int_{SOI}^{100^\circ} HRR\, d\theta} \quad (3)$$

With multiple injections, MFB can be broken up by its peaks and scaled to represent MFB *of each injection*, as shown in Figure 11. This is not ideal, since residual heat release from a prior injection can bleed into the next, but necessary to use MFB to evaluate ignition of each injection separately.

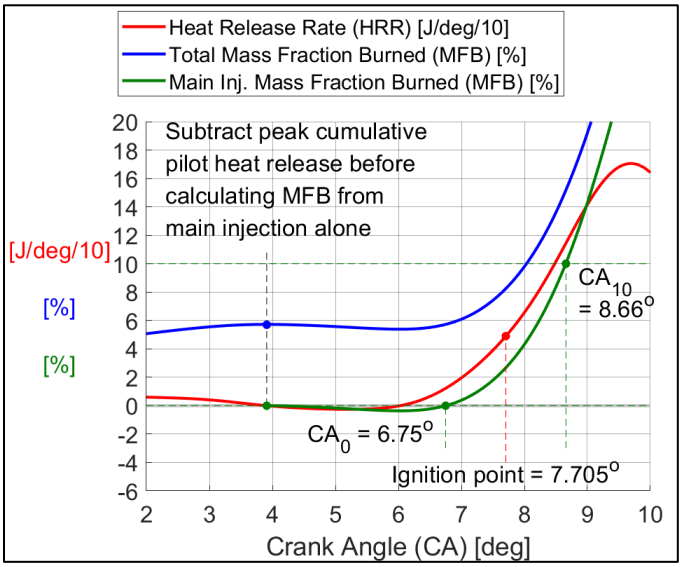

Figure 11. Example ignition point as determined by Method E. This matches, as closely as possible, the method used to determine the ignition point in the AFIDA ICN measurements from Table 1.

It is common practice to evaluate engine combustion phasing by the CA at which the MFB crosses a certain XX percentage of fuel burned, notated as CA_{XX}. CA_0 will be used as the analogue of ID_0 from the ICN method, with both representing the point where heat release from combustion has equaled and fully recovered the heat lost to evaporation. In the "typical signal output" figure for ICN tests given in ASTM D8183, the final pressure reached is about 1350 kPa above the baseline, which means that the 150 kPa threshold corresponds to approximately 10% of the heat released (when factoring in some heat loss and incomplete combustion in the test chamber). Thus, CA_{10} will be used as the analogue of ID_{150}, and this "ICN-imitating" method, referred to herein as Method E, will define the ignition point as the average of CA_0 and CA_{10}. These two points individually can also be used as definitions of ignition point and will both be included in the final comparisons.

Eliminating Outliers

Application of all these methods to individual cycles (rather than cycle-averaged data) often results in random failures to detect the correct ignition point. Pressure perturbations and signal noise vary greatly from cycle to cycle, which when combined with a constant *S* means that some cycles have unwanted peaks/threshold crossings that do not correspond with ignition, even in the smoothed data. To manually find and remove these failures would be impractical; instead, the data can be "cleaned" with an automatic outlier-rejection routine. This study uses the Median Absolute Deviation (MAD) [36] to do so:

$$\mathrm{MAD} = b * \mathrm{Median}(|\mathrm{ID}_i - \mathrm{Median}(\mathrm{ID}_i)|) \quad (5)$$

The constant b is based on the probability distribution of the data, with an assumed normal distribution (the assumption for this study)

corresponding to a value of 1.4826 for *b*. Outliers are rejected if lying more than a certain number of MAD from the median, with this study using the conservative value of 3 MAD as the rejection threshold. This study will also use *median* ignition delays as the primary test metric rather than mean (which can be skewed by outliers) with standard deviations taken from the "cleaned" data set with outliers removed.

Results

Ignition Point Location Relative to HRR Profile

The initial comparison of the methods uses cycle-averaged data from 100 cycles. This is done to present smooth HRR traces and track the detected ignition points. All methods are compared in Figure 12 over an SOI sweep of the D40 condition, the same condition used for the preceding demonstrations. The methods fall into two clusters: Methods A, D, and CA_0 find an ignition point at the base of the premixed autoignition phase, while Methods B, C and, CA_{10} find an ignition point on its upward slope, with Method E falling about halfway in between these two clusters. All methods are consistent in where the ignition point is found for the main injection. Ignition from the pilot injection is shown in more detail for an EGR sweep in Figure 13, which shows more pronounced LTHR and NTC. This shows that the upper cluster of methods is still consistent, but the lower cluster of methods is difficult to see. Figure 14 zooms in on this lower cluster.

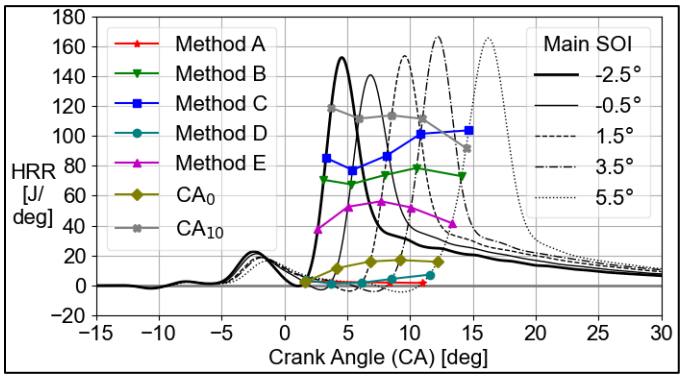

Figure 12. Comparison of main ignition point definition methods over a main injection SOI sweep of the D40 condition; cycle averaged results shown.

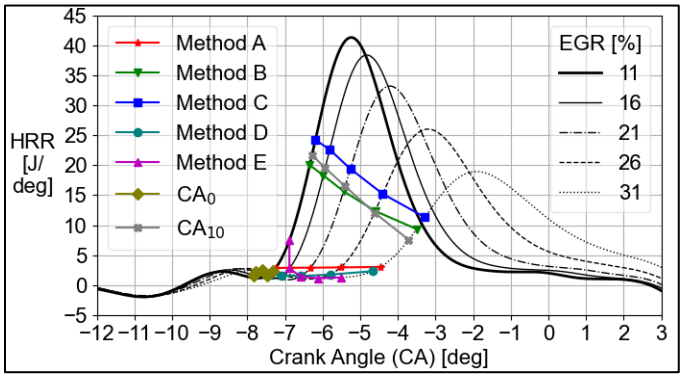

Figure 13. Comparison of pilot ignition point definition methods over an EGR sweep of the D40 condition; cycle-averaged results shown. Pilot SOI = -13.2°.

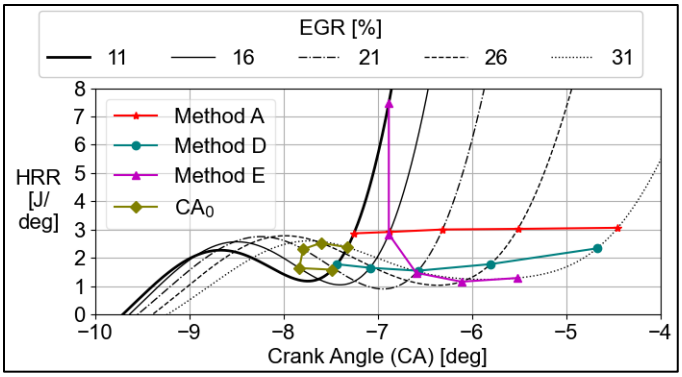

Figure 14. Comparison of pilot ignition point definition methods over an EGR sweep of the D40 condition. Zoomed-in view of Figure 13. Pilot SOI = -13.2°.

Figure 14 shows that calculation of CA_0 is affected by LTHR, which provides about the same amount of heat as the previous evaporative loss. At 11% EGR, the LTHR does not provide enough heat to recover the evaporative loss and CA_0 is found at the base of HTHR. However, at 16% EGR, NTC is retarded and more LTHR develops, speeding the recovery of evaporative loss. This advances CA_0, which when combined with the retard of CA_{10} causes the Method E ignition point to stay the same despite the clear ignition retard. This is a result of Method E imitating the ICN method, which appears to compute an average of LTHR and HTHR ID, based on the "typical output" chart in ASTM D8183. When testing fuels for MCCI performance in which LTHR is largely irrelevant, it may be worth considering alternative analyses of the raw ICN pressure trace to focus on just HTHR.

Comparing HRR Across Fuels/Test Conditions

To show a comparison of how ignition points change between fuels, Figure 15 plots the cycle-averaged HRR profiles for the base D40 condition with all 9 fuels from Table 1. These fuels are given their full identity in Figure 15; in the succeeding figures only the 4-letter abbreviations will be given to save space. Method D has been applied to both the pilot and main injections, finding both the start and end of autoignition for both. It is important to note that the main SOI occurs just after the end of the pilot autoignition, and if the main injection is advanced further toward the pilot, it will interfere with this point's detection. The SOI is used to assign the several points detected via Method D to particular injections, with Cantera simulations used to set 'break points' at half of the estimated cert ULSD ID after each SOI.

The HRR shapes can be explained by a conceptual model created from optical engine experiments by Dec [37]. The injection begins as a solid jet of fuel, but quickly undergoes jet breakup, atomization, and vaporization. This creates, at the point of ignition, a plume of air and fuel droplets/vapor in a rich mixture. The pilot injection in D40 ends before ignition, but the main injection does not, and will have a jet of fresh fuel mixing into the plume when it ignites. The rapid spike of heat release after ignition is called the premixed autoignition phase. The shorter the ID, the smaller the spike, as there is less time for fuel vapor to accumulate. A spike with a lower peak will lead to lower maximum pressure rise rates (MPRR). High MPRR can generate pressure waves that cause undesirable noise ('diesel knock') and put excess structural forces on engine components [38]. Pilot injections limit the MPRR of the main injection by raising temperature and lowering ID. Figure 15 illustrates how the height of the spike from the main injection is directly proportional to ID. On the other hand, the height of the *pilot* spikes show the opposite trend. This is because the pilot injections last less than half as long as ID, and there is thus enough time (and little enough fuel) for all these injections to mix completely.

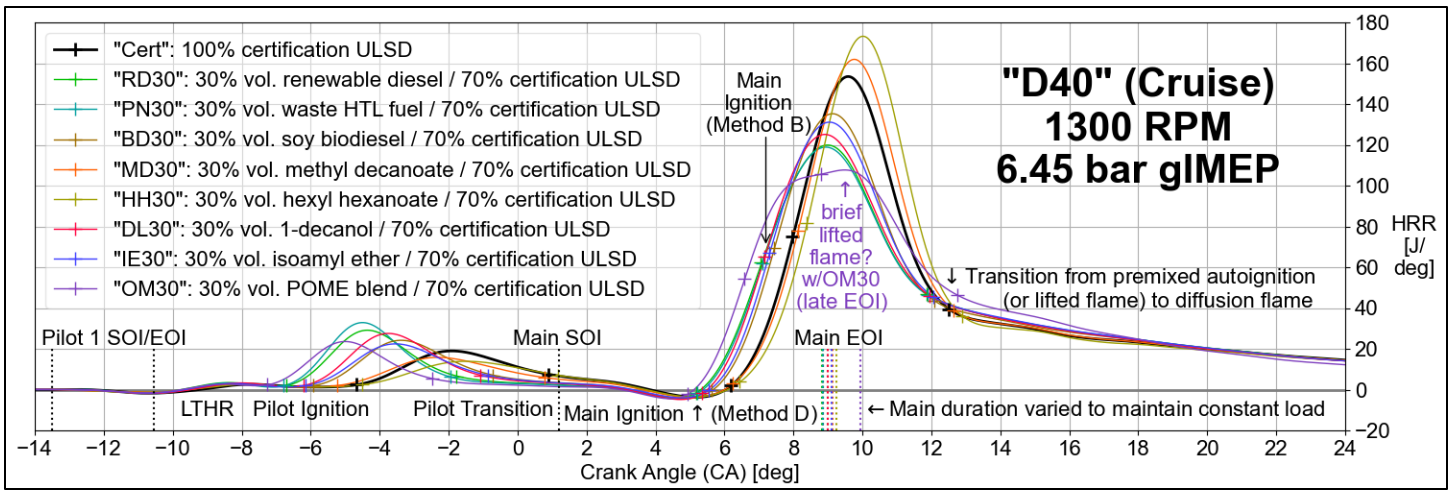

Figure 15. Cycle-averaged HRR profiles from the D40 condition with all fuel blends. Starts and ends of both premixed autoignition phases are found via Method D, with main injection ignition from Method B also shown for comparison. Method D picks up another point with the OM30 blend, hypothesized to be a brief transition from autoignition to a lifted flame, which only occurs with this particular blend due to its relatively early ignition and long duration.

With typical diesel conditions such as D40, ID is too short for the fuel to mix with air completely and local equivalence ratios are in the 2-4 range [37]. This leads to the formation of polyaromatic hydrocarbons (PAH's) and soot, which generate a diffusion flame at the periphery of the plume. The end of premixed autoignition and transition to diffusion is quantified by Method D with both injections and all fuels except one: the blend of 30% mixed POME in 70% ULSD, called "OM30" for short. This fuel had a high oxygen content (17%), more than 3 times that of any of the others (see Burton et al. [13]). This reduces LHV by 19% compared to ULSD and requires lengthening of the main injection to maintain constant load. Ideally the pilot injection duration would vary to keep constant heat of combustion in the pilot, but the measured fuel flow from the pilot was too small to set with sufficient precision, so pilot duration was kept constant. This is why the pilot spike from OM30 is significantly shorter than the nearby fuels in Figure 15.

The combination of short ID and long injection duration causes the main premixed phase to peak before the end of injection (EOI) with the OM30 blend, while the reverse is true for all the others. As a result, it appears there is still (briefly) an active fuel jet entering the plume when premixed autoignition peaks, which would trigger an additional hypothesized phase of MCCI: a standing rich premixed flame on the incoming fuel jet, lifted from the injector nozzle into the previous spray plume by the injection pressure [37]. This is difficult to verify with optical experiments due to the liquid spray and diffusion combustion surrounding it, but it provides a logical explanation for the increasing soot concentrations found downstream of the jet in long injections. It is therefore hypothesized that the additional Method D point detected in the OM30 HRR is a transition to a lifted flame.

The A20 condition, shown in Figure 16, features a similar departure of the OM30 main injection peak from the trend of the other fuels, although this departure is more subtle than D40 and no additional point is detected by Method D. This low-temperature condition features two pilots, with the main injection again ending very close to the premixed peak. The main ignitions are clustered very close together after the relatively large Pilot 1 injection, where ignition is more differentiated between fuels. The earlier and smaller Pilot 2 features even more differentiation, but this injection was so small relative to signal noise (and with a relatively large ratio of LTHR to HTHR) that it caused problems with all the ID methods, and is thus not used in any of the final evaluations in the following sections.

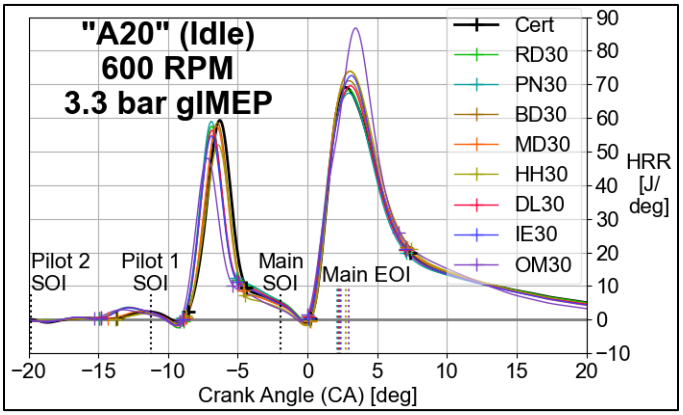

Figure 16. Cycle-averaged HRR profiles from the A20 condition with all fuel blends, with ignition and other key points produced by Method D.

The G60 condition, shown in Figure 17, is at a high enough load that the injector is not capable of delivering all the necessary fuel until well after the premixed autoignition is complete. This leads to a much more clearly defined lifted flame phase than the other two speed/load conditions, and a resulting transition point that is clearly detected by Method D with all the fuels. This phase ends near the modeled EOI for all fuels, leaving behind an already-established diffusion flame, again with the end of the phase reliably detected by the Method D.

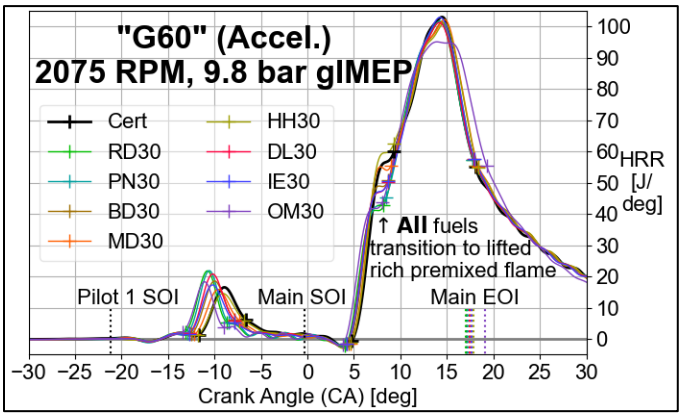

Figure 17. Cycle-averaged HRR profiles from the G60 condition with all fuel blends, with ignition and other key points produced by Method D.

Correlating Ignition Point Methods with CA_{50} and ICN

To test the reliability of all the ID methods on a cycle-by-cycle basis, the changes in cyclic ignition delay were correlated with changes in cyclic CA_{50}, with the resulting R_2 values given in Figure 18.

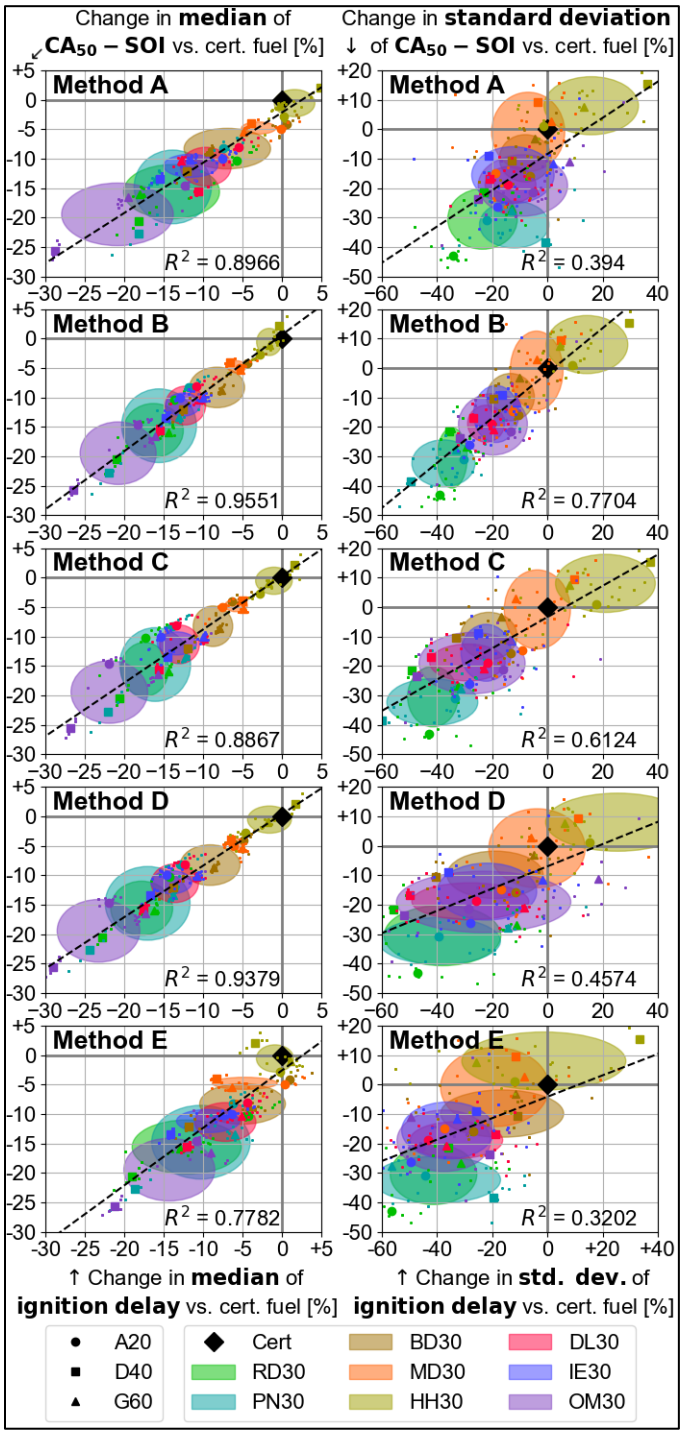

Figure 18. Correlations between changes in ignition delay (x-axis) and CA_{50} (y-axis), both measured as % change vs. cert ULSD. Small dots are individual data points, larger markers represent the average of each speed/load condition (Table 3), and shaded ellipses represent the range of each fuel (Table 1), with the center of the ellipse representing the average and the radii representing one standard deviation. The left column correlates the medians of the two variables, i.e. the median ID and CA50 of 100 cycles (minus outliers rejected via Equation 5). The right column correlates the standard deviations over those 100 cycles, again with outliers removed. Trendline and R^2 are for all data points.

In the left column of Figure 18, median ignition delay is correlated with median CA_{50}, which shows that Method E has poor correlation relative to the others. For this reason, combined with the issues seen previously in Figure 14, Method E will be ignored from here on. In the right column of Figure 18, the standard deviations of these same metrics (over however many of the 100 cycles recorded at each point remain following outlier removal) are correlated, to give an idea of how well cycle-to-cycle changes are being tracked. While a reduced ID in an individual cycle may not necessarily change CA_{50}, a relatively inconsistent ID should produce a relatively inconsistent CA_{50}. This correlation helps to confirm that cycle-to-cycle changes in the detected ignition point represent real changes in ID, rather than randomness in where the method detects the ignition point. In this regard, Method B clearly outperforms the others, which makes it the preferred method in this study for analyzing cycle-to-cycle variance of ID.

Another way to compare these methods is the correlation with ICN, shown in Figure 19 for Methods A-D. Method B has the lowest R^2 of these correlations, which does not mean it is poorest representation of ID but counters its relatively strong correlation with CA_{50} from Figure 18. Given the lack of differentiation between these four methods, the preferred method for measuring absolute ID in the rest of this work will be Method D, on the merit of its location at the base of the HRR spike and its additional capabilities of detecting the other MCCI ignition points, as well as ignition of other combustion modes [34].

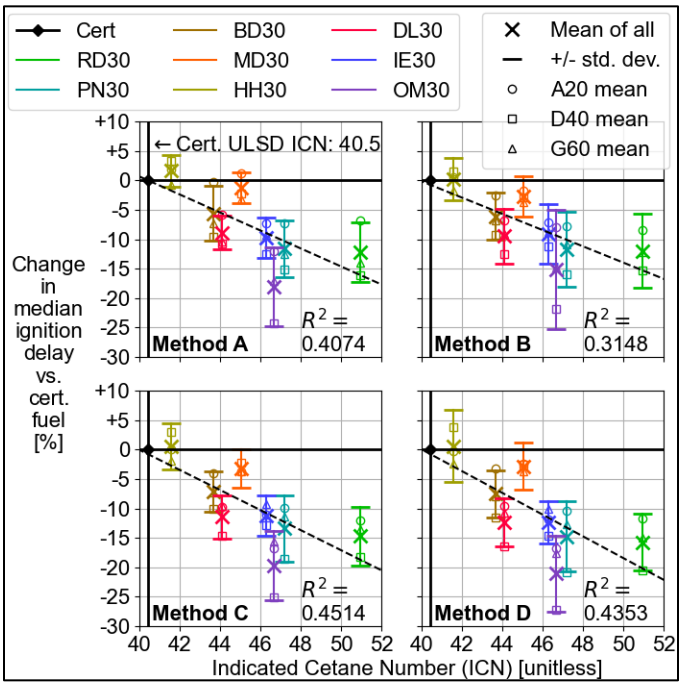

Figure 19. Correlations between ICN and engine ID using four different ignition point methods, using all test points.

According to Figure 19, the blend of 30% methyl decanoate (MD30) under-performs ICN while two other blendstocks with similar chemical structures provide more ID reduction despite lower ICN. The biodiesel blendstock used in BD30 was commercially produced and its exact composition is unknown, but based on average soy biodiesel composition [39], it should contain mostly methyl esters like methyl decanoate, but with carbon chains of 16-18 atoms compared to 10 atoms in decanoate. Meanwhile the 1-decanol blendstock in DL30 shares the 10-carbon chain of the decanoate but has a hydroxyl group at its end instead of an ester group. Unlike the BD30 and DL30, the hexyl hexanoate in HH30 had almost the same ID as MD30, but did so with an ICN much lower than MD30. The primary difference between these two blendstocks, which are both pure ester compounds, is the location of the ester group. With the methyl decanoate, the ester group

is at the end of the molecule, with 10 carbons on one side and one on the other, while the hexyl hexanoate has the ester group in the middle, with 6 carbons on each side. This transposition has a large effect on ICN, but a negligible effect on ID. The blends from the two ether blendstocks had very similar ICN, but in terms of ID reduction the POME mixture in OM30 outperformed the isoamyl ether in IE30. The highly-oxygenated OM30 even outperformed the two hydrocarbon mixtures of PN30 and RD30, despite them both having higher ICN. The hydroprocessed ester and fatty acid (HEFA) renewable diesel in RD30 was also commercially produced and its exact composition unknown, but is assumed to contain mostly alkanes [40], and the waste HTL fuel in PN30 was composed primarily of alkanes, as confirmed by spectral analysis [13]. There was no significant change in ignition delay between the two hydrocarbon blends, despite a difference of 4 in ICN.

Ignition Delay Changes over SOI and EGR Sweeps

The wide error bars in Figure 19 show that ID varies widely over the parameter sweeps of SOI and EGR, as does the percentage of change in ID vs. the baseline fuel. This can be seen by plotting ID over these sweeps, which is done for a select few sweeps in Figure 20 and Figure 21. These figures show both median and standard deviation of ID using different preferred methods – Method D for median, and Method B for standard deviation – for the reasons discussed in the previous section.

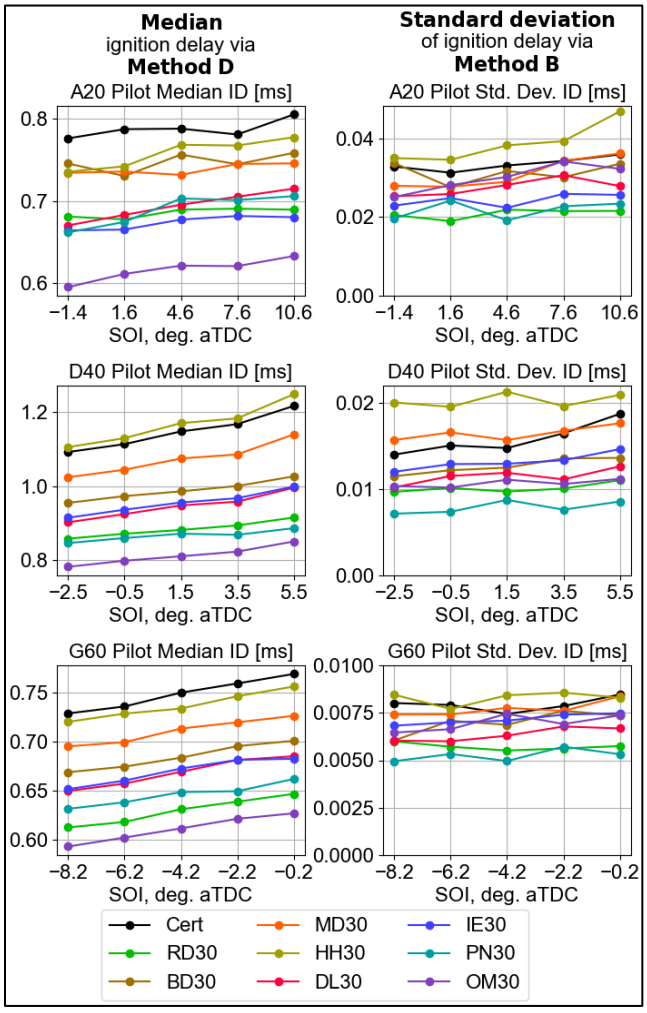

Figure 20. Pilot injection ID over SOI sweeps of all 3 speed/load conditions.

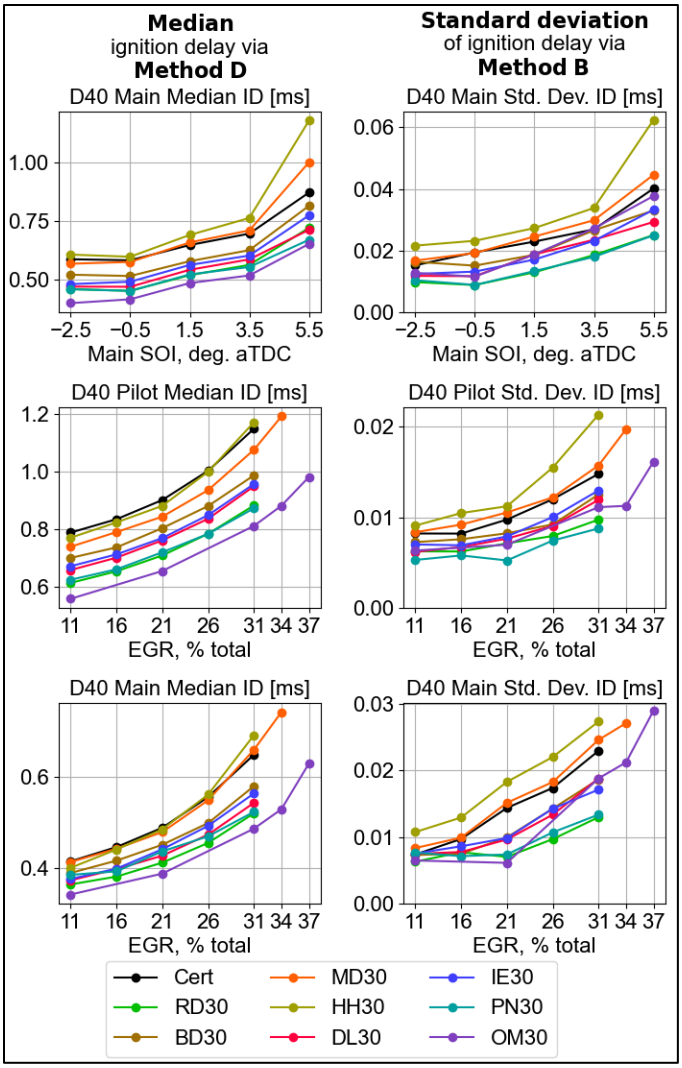

Figure 21. D40 ID for main (top and bottom) and pilot (middle) injections over sweeps of main injection SOI (top) and EGR (middle and bottom).

Figure 20 collects the ID of the pilot injections of all 3 speed/load conditions over their respective SOI sweeps; these sweeps show the lowest sensitivities of ID to the swept parameter and best illustrate the level of separation between the fuels. The standard deviation is quite low compared to median: in the most extreme case of HH30 in A20, the standard deviation is only 6% of the median, which drops to 2% in D40 and 1% in G60. Other methods besides B did not change the magnitude of these standard deviations noticeably. This is very promising since all of the blends seem to provide acceptably stable ignition, but another thing to consider is that the percentage of separation between the fuels relative to the baseline is much greater in the standard deviation than in the median. There is about 20-30% separation between the slowest- and quickest-igniting fuels in each speed/load condition, but 40-60% separation in their standard deviation. There is also one fuel that shifts its position relative to the others significantly when switching from median to standard deviation: the OM30 blend, which had the lowest median ID in every case, but a standard deviation closer to the middle of the pack.

Figure 21, by contrast to Figure 20, shows the sweeps with the highest sensitivity to the swept parameter: the other three sweeps from the D40 condition, i.e. the main injection ID over the SOI sweep and the ID of both injections over the EGR sweep. The EGR sweep was extended for the MD30 and OM30 fuels to explore the extremes of EGR these fuels could tolerate before generating excessive soot (see Burton et al. [13]). These plots show how the relative ID of the fuels begins to

diverge at the far right of each sweep, where conditions become the coldest (SOI sweep) and most dilute/oxygen-deprived (EGR sweep). The HH30 fuel in particular shows signs of degrading performance at the end of the sweep, which is unfortunate since reaching the end of these sweeps will provide substantial NO_X reductions as demonstrated in the companion study [13]. The most promising find here is that most of the biofuel blends increase the tolerance of ID to EGR substantially: in the most extreme case, OM30 shows lower median ID at 37% EGR than the ULSD does at 26% EGR, and although its standard deviation of ID increases, it is still less than 2% of the median.

Overall Ignition Delay/Combustion Phasing Changes

To collect all of the test data into a single plot, Figure 22 shows shaded ellipses that are centered around the average of all the test conditions for a particular fuel, with radii on each axis equal to one standard deviation. Also shown are markers at the average of each of the three speed/load conditions. The change in the median ID (via Method D) is on the x-axis, with the coefficient of variation (COV, standard deviation divided by the median) on the y-axis. This highlights how the hydrocarbon blends (RD30 and PN30) exhibit not just faster ignition, but more stable ignition as well, with COV reductions over the baseline about twice as great, percentagewise, as the reductions in the median. On the other side, the hexyl hexanoate blend (HH30) makes ID *less* stable, particularly in the D40 condition. The general trend is that drops in median ID correlate with greater drops in COV of ID, but OM30 does not fit this trend. Despite providing the largest drop in median ID, OM30 does not improve COV of ID at all.

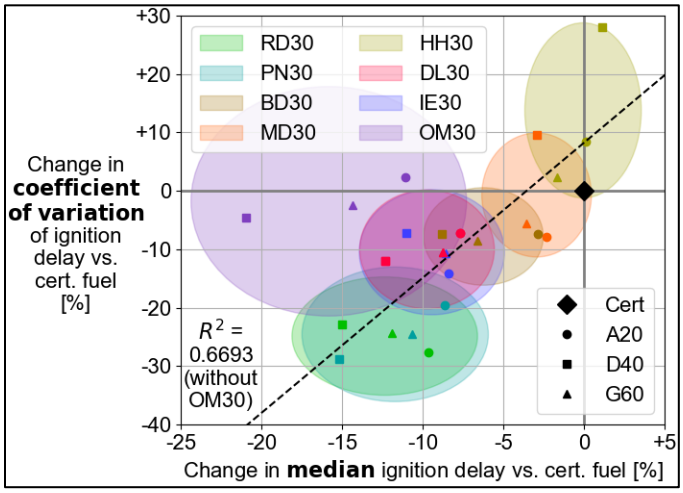

Figure 22. Correlations between changes in median ID (x-axis) and COV of ID (y-axis), both measured as % change vs. cert ULSD. Markers represent the average of each speed/load condition (Table 3), and shaded ellipses represent the range of each fuel (Table 1), with the center of the ellipse representing the average and the radii representing one standard deviation.

Besides ID, there are other aspects of MCCI combustion phasing that can be evaluated across these fuels. Method D tracks the end of the premixed autoignition phase as well as its start, allowing evaluation of the changes in the duration of this phase. These changes are highly correlated with changes in the median ID, with duration being reduced over the baseline about half as much as ID with great consistency. A more interesting aspect of MCCI phasing that did not have such a simple correlation with ID was the duration of the entire process, which is defined here as the gap between CA_{10} and CA_{90}, or $CA_{10\text{-}90}$. Changes in these two durations are plotted in Figure 23, using the same style as Figure 22. There is a general trend that reductions in premixed autoignition duration (and thereby reductions in ID, which are highly correlated) lead to *increases* in the overall combustion duration. This in undesirable from an efficiency perspective, as delayed heat release results in lost work at the top of the power stroke. Once again, OM30 breaks this trend, but this time in a positive way. Despite having the greatest reduction in ID, OM30 also had the greatest reductions in overall duration, which may explain why it also has the greatest gross indicated thermal efficiency (gITE) as reported in the companion study [13]. However, this may be due to the hypothesized brief lifted flames in A20 and D40 that were only observed with OM30.

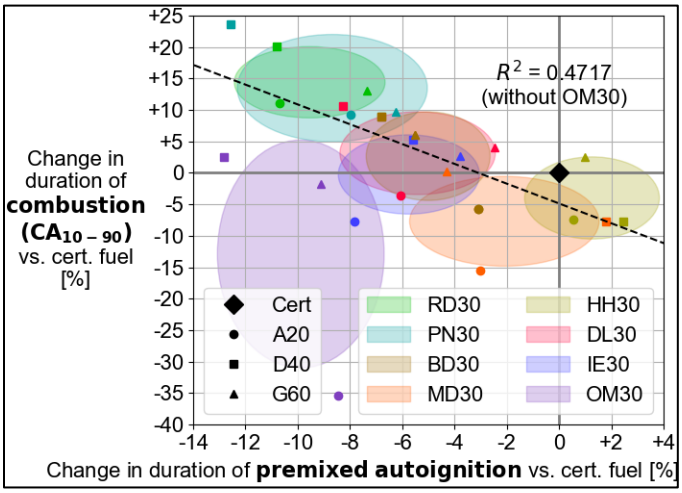

Figure 23. Correlations between changes in duration of autoignition (x-axis) and duration of combustion as $CA_{10\text{-}90}$ (y-axis), both measured as % change vs. cert ULSD. Markers represent the average of each speed/load condition (Table 3), and shaded ellipses represent the range of each fuel (Table 1), with the center representing the average and the radii representing one standard deviation.

With the reduced LHV and increased injection duration of OM30, fuel energy is entering the combustion chamber at a significantly lower rate than with the other fuels. If only LHV was changing, this would retard CA_{50} and increase combustion duration, but instead CA_{50} is advanced and duration is reduced. The reduced ID does not explain the advance of CA_{50}, which occurs after the premixed autoignition phase, and should also increase combustion duration by advancing CA_{10}. This suggests that the OM30 fuel is both igniting more quickly *and* progressing through the MCCI process more quickly once it ignites, possibly due to its low sooting tendency and/or high oxygen content. This is the only fuel whose LHV and injection duration differ greatly enough from the baseline greatly enough make such observations.

Effect on Maximum Pressure Rise Rate/Knock

One advantage of reduced ID is reduction in maximum pressure rise rate (MPRR), which can generate excessive engine noise ("diesel knock") and raise the structural forces on engine components [38]. MPRR is plotted over the SOI sweep of D40 in Figure 24, which shows how the most advanced SOI has roughly the same ID as the 2nd-most advanced SOI for all fuels, but a much higher MPRR. This is due to the premixed autoignition spike in the HRR occurring close to TDC, where heat release will raise pressure most rapidly due to the minimal volume. Retarding SOI further will have competing effects: moving premixed autoignition away from TDC will reduce MPRR due to the increase in volume, but will also reduce temperature, increasing ID. This allows more fuel vapor to accumulate before ignition, resulting in a taller HRR spike and a higher MPRR. These two effects cancel each other out initially, but as SOI is retarded, one of these effects may begin to dominate. With the highest-ID fuels, the effect of reduced temperature dominates, and MPRR falls toward the end of the sweep.

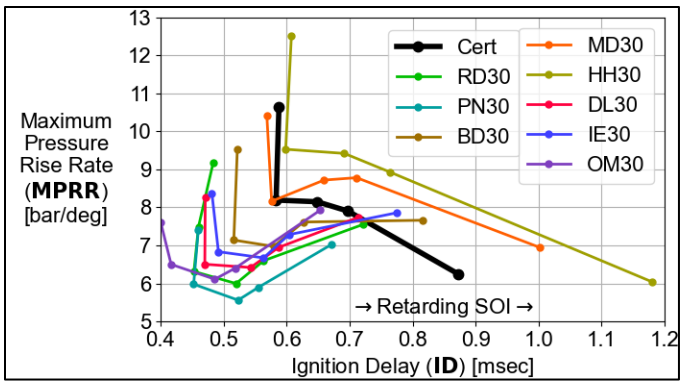

Figure 24. ID/MPRR trade-off at the D40 operating condition (1300 rpm, 6.45 bar gIMEP), SOI sweep data shown.

Conversely, with the lowest-ID fuels, the effect of increased fuel accumulation dominates, and MPRR rises toward the end of the sweep. Figure 25 switches the x-axis to CA_{50} to illustrate how this disparity only appears at the late end of the sweep, with the trend matching across fuels in the earlier part of the sweep.

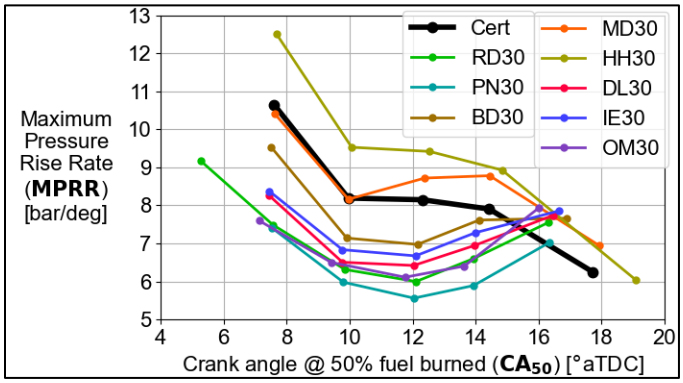

Figure 25. CA_{50}/MPRR trade-off at the D40 operating condition (1300 rpm, 6.45 bar gIMEP), SOI sweep data shown.

In the EGR sweep, shown in Figure 26, different effects dominate at different levels of EGR. At the lowest EGR level, there is a very sharp inverse relationship between ID and MPRR at the earliest ID, seen only with the lowest-ID fuels. Since EGR does not change CA_{50} as much as SOI, this may be due to either the advanced location of the premixed spike *or* the lack of dilution from EGR to slow down combustion and lower the height of the spike. Adding EGR initially achieves reduced MPRR, but at high EGR, increased fuel accumulation dominates and MPRR goes back up. The lowest-ID fuels tolerate more EGR before this happens, seen in Figure 27 where the x-axis is switched to EGR.

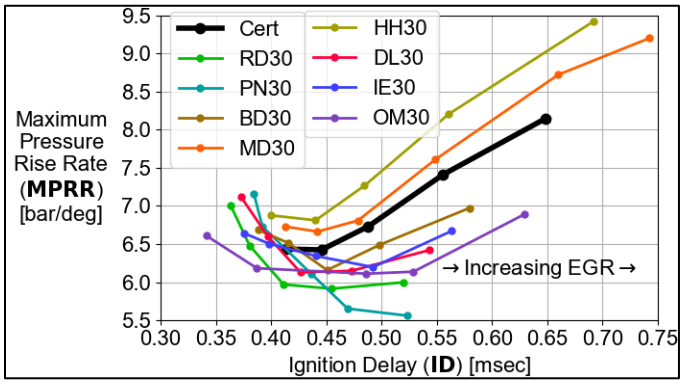

Figure 26. ID/MPRR trade-off at the D40 operating condition (1300 rpm, 6.45 bar gIMEP), EGR sweep data shown.

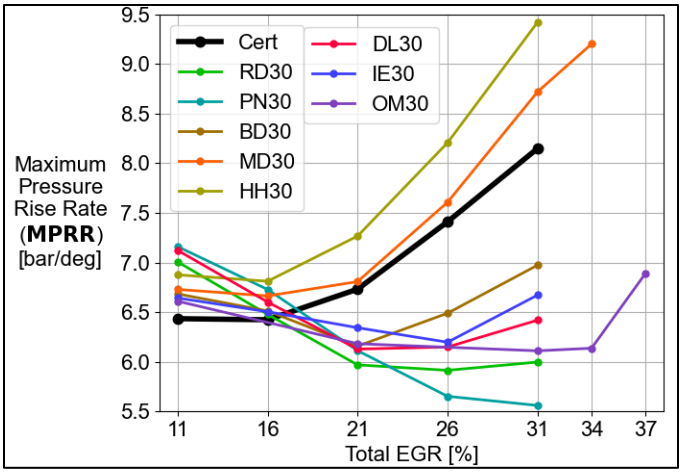

Figure 27. EGR vs. MPRR trade-off at the D40 operating condition (1300 rpm, 6.45 bar gIMEP).

Summary/Conclusions

After reviewing the methods of determining MCCI ignition delay from engine cylinder pressure and applying the most robust methods to a set of experiments with biofuel/ULSD blends, key findings include:

- Careful smoothing and derivation of the cylinder pressure signal must be applied to obtain reliable ID measurements on individual cycles of pressure data.
- Of the methods examined, four were found equally reliable in measuring median-cycle ID changes with the biofuels.
- Some methods define ignition at a point approximately halfway up the premixed autoignition spike of the HRR, while others define ignition at the *base* of this spike, and this dissonance may prevent effective cross-study comparisons.
- Method D is preferred to analyze *median cycle* ID trends because of its consistent location at the base, while also detecting other key points in the MCCI process.
- Method B is preferred to analyze *variance* of ID from cycle-to-cycle because of its high correlation with variance in CA_{50} compared to the other methods.
- All eight biofuel blends show either no significant change or significant reductions in median ID, with the esters showing less reduction than the ethers, alcohol, and hydrocarbons.
- ICN is only somewhat reliable in predicting these changes, with the methyl decanoate blend most significantly under-performing its ICN and the POME blend over-performing it.
- In general, reductions in median ID correlate with reductions in the variance of ID, particularly with the hydrocarbons.
- The POME blend breaks this trend, having no significant change in ID variance despite great median ID reductions.
- The POME blend appears to reduce combustion duration even despite its reduced ID, reduced LHV, and the increased main injection duration necessary to maintain constant load.
- In all cases, variance of ID is small compared to magnitude, except in extreme cases of high SOI retard and high EGR.
- The reductions in ID lead to significant reductions in MPRR in most cases but will have nonlinear effects when highly retarded SOI or low levels of EGR are used.

All 8 of the biofuel blendstocks tested herein exhibit acceptably low and stable ignition delays at a 30% blend level with ULSD, which when combined with their favorable NO_X, soot, and efficiency results from the companion study [13] makes them promising candidates for drop-in, low-carbon CI engine fuel in the near future.

References

1. Myhre, G., Shindell, D., Bréon, F.-M., Collins, W. et al.: "Anthropogenic and Natural Radiative Forcing," In: *Climate Change 2013: The Physical Science Basis. Contribution of Working Group I to the Fifth Assessment*, (Cambridge, UK, Cambridge University Press, 2013), 661, https://www.ipcc.ch/site/assets/uploads/2018/02/WG1AR5_Chapter08_FINAL.pdf, accessed Nov. 2020.
2. BP, "BP Statistical Review of World Energy," 2019, http://www.bp.com/content/dam/bp/business-sites/en/global/corporate/pdfs/energy-economics/statistical-review/bp-stats-review-2019-full-report.pdf, accessed Oct. 2020.
3. Conti, J., Holtberg, P., Diefenderfer, J., LaRose, A. et al., "International Energy Outlook 2016 With Projections to 2040," 2016, doi:10.2172/1296780.
4. Field, J. L., Richard, T. L., Smithwick, E. A., Cai, H., "Robust paths to net greenhouse gas mitigation and negative emissions via advanced biofuels," *P. Natl. Acad. Sci. USA* 117(36):21968-21977, 2020, doi:10.1073/pnas.1920877117
5. Uría-Martínez, R., Leiby, P. N., Brown, M. L., "Energy security role of biofuels in evolving liquid fuel markets," *Biofuel Bioprod. Biorefin.* 12(5):802-814, 2018, doi:10.1002/bbb.1891
6. International Energy Agency, "Global EV Outlook 2020," 2020, http://www.iea.org/reports/global-ev-outlook-2020, accessed Oct. 2020.
7. Tartaglia, K., Birky, A., Laughlin, M., Price, R. et al., "Transportation Electrification Beyond Light Duty: Technology and Market Assessment, Report No. ORNL/TM-2017/77-R1, Oak Ridge National Lab (ORNL), 2017, doi:10.2172/1413627.
8. Wallington, T. J., Lambert, C. K., Ruona, W. C., "Diesel vehicles and sustainable mobility in the US," *Energy policy* 54, :47-53, 2013, doi:10.1016/j.enpol.2011.11.068
9. Dec, J. E., "Advanced compression-ignition engines—understanding the in-cylinder processes," *P. Combust. Inst.* 32(2):2727-2742, 2009, doi:10.1016/j.proci.2008.08.008
10. Lu, X., Han, D., Huang, Z., "Fuel design and management for the control of advanced compression-ignition combustion modes," *Prog. Energ. Combust. Sci.* 37(6):741-783, 2011, doi:10.1016/j.pecs.2011.03.003
11. Dempsey, A. B., Walker, N. R., Gingrich, E., Reitz, R. D., "Comparison of low temperature combustion strategies for advanced compression ignition engines with a focus on controllability," *Combust. Sci. Technol.* 186(2):210-241, 2014, doi:10.1080/00102202.2013.858137
12. Mueller, C., "Mixing-Controlled Compression-Ignition Combustion: What It Is Fuel Effects and Prospects for the Future," Report no. SAND2018-1509PE-660652, Sandia National Laboratories (SNL), 2018, http://www.https://www.osti.gov/biblio/1495784, accessed Oct. 2020.
13. Burton, J. L., Martin, J. A., Fioroni, G. M., Alleman, T. L. et al., "Fuel Property Effects of a Broad Range of Potential Biofuels on Mixing Control Compression Ignition Engine Performance and Emissions," Submitted for publication at SAE World Congress 2021.
14. Dallmann, T., Posada, F., Bandivadekar, A., "Costs of Emission Reduction Technologies for Diesel Engines Used in Non-Road Vehicles and Equipment," Working Paper 2018-10, International Council on Clean Transportation, 2018, https://theicct.org/sites/default/files/publications/Non_Road_Emission_Control_20180711.pdf, accessed Nov. 2020.
15. Yanowitz, J., Ratcliff, M. A., McCormick, R. L., Taylor, J. D., "Compendium of experimental cetane numbers," Report no. NREL/TP-5400-6758, National Renewable Energy Laboratory (NREL), 2017, doi:10.2172/1345058.
16. Rothamer, D. A., Murphy, L., "Systematic study of ignition delay for jet fuels and diesel fuel in a heavy-duty diesel engine," *P. Combust. Inst.* 34(2):3021-3029, 2013, doi:10.1016/j.proci.2012.06.085
17. Assanis, D. N., Filipi, Z. S., Fiveland, S. B., Syrimis, M., "A predictive ignition delay correlation under steady-state and transient operation of a direct injection diesel engine," *J. Eng. Gas Turbines Power* 125(2):450-457, 2003, doi:10.1115/1.1563238
18. Shahabuddin, M., Liaquat, A. M., Masjuki, H. H., Kalam, M. A. et al., "Ignition delay, combustion and emission characteristics of diesel engine fueled with biodiesel," *Renew. Sustain. Energy Rev.* 21:623-632, 2013, doi:10.1016/j.rser.2013.01.019
19. Fioroni, G., Fouts, L., Luecke, J., Vardon, D. et al., "Screening of potential biomass-derived streams as fuel blendstocks for mixing controlled compression ignition combustion," *SAE Int. J. Adv. Curr. Pract. Mobil.* 1(3):1117-1138, 2019, doi:10.4271/2019-01-0570
20. Stein, Y., Yetter, R. A., Dryer, F. L., Aradi, A., "The autoignition behavior of surrogate diesel fuel mixtures and the chemical effects of 2-ethylhexyl nitrate (2-EHN) cetane improver," *SAE Transactions* 108(4):1027-1045, 1999, doi:10.4271/1999-01-1504
21. Bodisco, T. A., Pham, P. X., Islam, A., Brown, R. J. et al., "Ignition delay of bio-fuels in a common-rail compression ignition engine," Australian Combustion Symposium, Perth, Australia, 2013, https://eprints.qut.edu.au/65267/, accessed Nov. 2020.
22. Zheng, M., Mulenga, M. C., Reader, G. T., Wang, M. et al., "Biodiesel engine performance and emissions in low temperature combustion." *Fuel* 87(6):714-722, 2008, doi:10.1016/j.fuel.2007.05.039
23. ASTM International, "Standard Test Method for Cetane Number of Diesel Fuel Oil," ASTM Standard D613, Rev. Jan. 2019, doi:10.1520/D0613-18A
24. Abel, R. C., Luecke, J., Ratcliff, M. A., Zigler, B. T., "Comparing cetane number measurement methods," ASME 2020 International Combustion Engine Fall Technical Conference, Denver, CO, Nov. 1-4 2020.
25. Zacher, A., Elliott, D., Olarte, M., Wang, H. et al., "Technology advancements in hydroprocessing of bio-oils," *Biomass and Bioenergy* 125:151-168, 2019, doi:10.1016/j.biombioe.2019.04.015
26. "Process Development Units," Pacific Northwest National Laboratory (PNNL), https://www.pnnl.gov/process-development-units, accessed Nov. 2020
27. Kass, M., Wissink, M., Janke, C., Connatser, R., "Compatibility of Elastomers with Polyoxymethylene Dimethyl Ethers and Blends with Diesel," SAE Technical Paper 2020-01-0620, 2020, doi:10.4271/2020-01-0620.
28. ASTM International, "Standard test method for determination of indicated cetane number (ICN) of diesel fuel oils using a constant volume combustion chamber—reference fuels calibration method," ASTM Standard D8183, Rev. May 2018, doi:10.1520/D8183-18
29. de Boor, C., "A Practical Guide to Splines," *Mathematics of Computation* 34(149):325, 1980, doi:10.2307/2006241
30. Heywood, J., "Internal Combustion Engine Fundamentals," (New York, McGraw-Hill, 1988), 510, isbn:978-0-07-028637-5
31. Sauer, T., "Numerical Analysis," (Boston, Pearson, 2012), 250, isbn:978-0-321-78368-4
32. Luecke, J., Rahimi, M. J., Zigler, B. T., Grout, R. W., "Experimental and numerical investigation of the Advanced Fuel Ignition Delay Analyzer (AFIDA) constant-volume combustion chamber as a research platform for fuel chemical kinetic mechanism validation," *Fuel* 265:116929, 2020, doi:10.1016/j.fuel.2019.116929

33. Mueller, C.: Sandia National Laboratories (SNL), personal communcation, Aug. 2020.
34. Ortiz-Soto, E. A., Lavoie, G. A., Martz, J. B., Wooldridge, M. S., "Enhanced heat release analysis for advanced multi-mode combustion engine experiments," *Applied energy* 136:465-479, 2014, doi:10.1016/j.apenergy.2014.09.038
35. Kline, M., "Calculus: An Intuitive and Physical Approach," (Mineola, NY, Dover, 1998), 457, isbn:978-0-486-40453-0
36. Leys, C., Ley, C., Klein, O., Bernard, P., "Detecting outliers: Do not use standard deviation around the mean, use absolute deviation around the median," *J. Exp. Soc. Psychol.* 49(4):764-766, 2013, doi:10.1016/j.jesp.2013.03.013
37. Dec, J., "A conceptual model of DL diesel combustion based on laser-sheet imaging," *SAE Transactions* 106(3):1319-1348, 1997, doi:10.4271/970873
38. Schaberg, P., Priede, T., Dutkiewicz, R., "Effects of a rapid pressure rise on engine vibration and noise," SAE Technical Paper 900013, 1990, doi:10.4271/900013.
39. Clemente, T. E., Cahoon, E. B., "Soybean Oil: Genetic Approaches for Modification of Functionality and Total Content," *Plant Physiology* 151(3):1030-1040, 2009, doi:10.1104/pp.109.146282
40. Vozka, P., Šimáček, P., Kilaz, G., "Impact of HEFA feedstocks on fuel composition and properties in blends with jet A," *Energy & Fuels* 32(11):11595-11606, 2018, doi:10.1021/acs.energyfuels.8b02787

Contact Information

Corresponding Author: Dr. Jonathan A. Martin, Postdoctoral Researcher, Fuels and Combustion Science, National Renewable Energy Laboratory (NREL), 15013 Denver West Parkway, Golden, CO 80401, Phone: 303-275-4581, jonathan.martin@nrel.gov

Acknowledgments

Research at the National Renewable Energy Laboratory was performed under Contract DE347AC36-99GO10337 as part of the Co-Optimization of Fuels & Engines (Co-Optima) project sponsored by the US Department of Energy – Office of Energy Efficiency and Renewable Energy, Bioenergy Technologies and Vehicle Technologies Offices. The views expressed in the article do not necessarily represent the views of the US Department of Energy or the US Government. The US Government retains and the publisher, by accepting the article for publication, acknowledges that the US Government retains a nonexclusive, paid-up, irrevocable, worldwide license to publish or reproduce the published form of this work, or allow others to do so, for US Government purposes.

The authors also thank Eric Kurtz and colleagues at Ford Motor Company for their support with the engine design and configuration.

Definitions/Abbreviations

AHRR	apparent heat release rate
AFIDA	Advanced Fuel Ignition Delay Analyzer
CA	crank angle
CI	compression-ignition
CN	cetane number
COV	coefficient of variance
DAQ	data acquisition
ECU	engine control unit
EGR	exhaust gas recirculation
EOI	end of injection
EVC	exhaust valve closing
EVO	exhaust valve opening
gITE	gross indicated thermal efficiency
HCCI	homogeneous charge compression ignition
HEFA	hydroprocessed esters and fatty acids
HOV	heat of vaporization
HRR	heat release rate
HTHR	high temperature heat release
HTL	hydrothermal liquefaction
ICN	indicated cetane number
ID	ignition delay
IVC	intake valve closing
IVO	intake valve opening
LHV	lower heating value
LTHR	low temperature heat release
MAD	median absolute deviation
MCCI	mixing-controlled compression igntion
MFB	mass fraction burned
MPRR	maximum pressure rise rate
NOx	nitric oxides
NTC	negative temperature coefficient
OEM	original equipment manufacturer
PAH	polyaromatic hydrocarbons

PNNL	Pacific Northwest National Laboratory
POME	polyoxymethylene ethers
PRF	primary reference fuel
SACI	spark-assisted compression ignition
SOI	start of injection
TDC	top dead center
ULSD	ultra-low-sulfur diesel
b	probability distribution coefficient
cor	(subscript) corrected
E	error
fired	(subscript) taken from a fired engine cycle
h	step size
k	curvature
motor	(subscript) taken from a motoring engine cycle
nor	(subscript) normalized
p	pressure
Q	heat
S	smoothing parameter
V	volume
γ	ratio of specific heats
θ	crank angle